Fold propagation in tapered-springs: Part I

J A Clarkson & K A Seffen

Advanced Structures Group, Civil Engineering Building, Department of Engineering, University of Cambridge, CB3 0FA

jac287@cam.ac.uk & kas14@cam.ac.uk

Abstract

Many elastic systems can localise during deformation into co-existent modes, or "phases", of lower and higher strain; further deformation is accommodated by growth of the high-strain phase at a constant load, which is sometimes declared a "propagating instability". The strains in each phase can be obtained from applying the Maxwell Equal-Areas Construction to the generalised stress-strain relationship, which must be satisfied on the boundary between the phases. If the elastic domain has a spatially varying stress-strain relationship, this can reveal interesting behaviour: in particular, we investigate systems with spatially varying stress-strain relationships using "folded" tape-springs with varying cross-section geometry. Two special cases are considered in which the geometry varies systematically: "constant-α" and "constant-b" springs. These form folds which are spiral in shape, in contrast to the constant curvature fold in a standard tape-spring. These concepts may have beneficial application in designing new deployable structures.

Keywords: localisation, phase, Maxwell Construction, varying stress-strain relationship, tape-spring folds

Major nomenclature

$\sigma =$ generalised stress
$\epsilon =$ generalised strain
$u =$ strain energy per unit length
$U =$ total strain energy
$r =$ transverse radius of relaxed tape
$\alpha =$ angle subtended by tape cross-section
$b =$ transverse width of tape, equal to $r\alpha$
$h =$ thickness of tape
$E =$ Young's modulus
$\nu =$ Poisson's ratio
$D =$ plate flexural stiffness, $Eh^3/12(1-\nu^2)$
$\kappa_x =$ longitudinal curvature
$\kappa_y =$ transverse curvature
$M =$ section bending moment, parallel to y axis
$m =$ dimensionless bending moment, m/D
$L =$ tape-spring length
$L_f =$ tape-spring fold length
$\Theta =$ total angle subtended in bending, equal to $\int \kappa_x \, \mathrm{d}x$
$T =$ dimensionless parameter comparing beam-like versus plate-like bending, $\sqrt{b^2/rh}$
$\xi =$ dimensionless parameter relating κ_x to κ_{y0} on the propagating front of the fold, κ_{y0}/κ_x

1 Introduction

Many elastic systems exhibit localisation, where, under displacement control, uniform deformation gives way to deformation divided into two distinct regions, or *phases*, of differing strain, with growth, sometimes called "propagation", of the high-strain region at a constant load. Examples include the inflation of long balloons [1], the buckling of beams on non-linear elastic foundations [2], and the folding of tape-springs [3], to which particular reference will be made in this paper. Common to these systems is a characteristic "up-down-up" relationship between the problem-specific work-conjugate variables, e.g. stress-strain or moment-curvature. Here, we turn our attention to elastic systems where the stress-strain relationship varies spatially throughout the domain. Variation in elastic properties can be found in naturally occurring materials such as honeycombs and wood [4], as well as in manufactured materials such as engineered foams [5], which contain bubbles of different shapes and sizes; the variation is typically random and, on a large scale, relatively homogeneous. By contrast, in so-called "meta-materials", which form unit cells via additive manufacturing methods, variation can be engineered in a controlled manner by changing the unit cell architecture, resulting in large scale heterogeneity in elastic properties [6]; we focus on localisation in one-dimensional heterogeneous systems, and show that this leads to a non-uniform high-strain phase which propagates at a varying load.

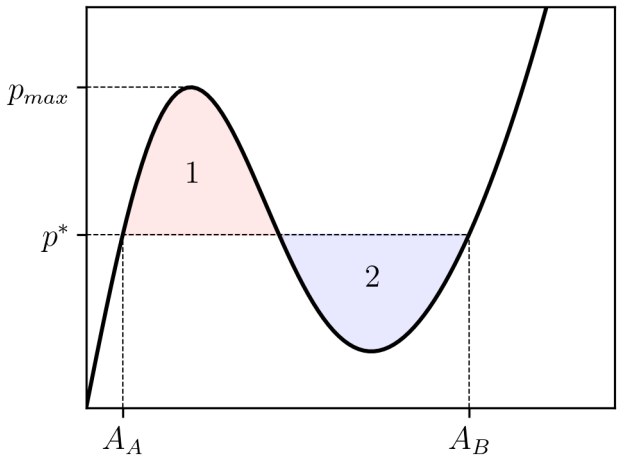

Figure 1: Balloon pressure-cross-sectional area relationship, with Maxwell Equal-Areas construction illustrated.

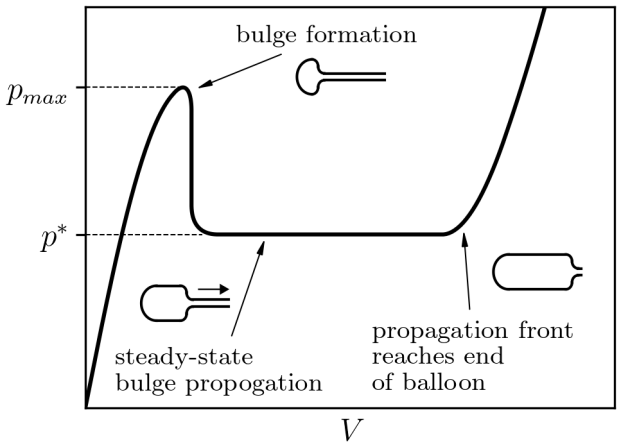

Figure 2: Balloon pressure-volume relationship during inflation

However, before investigating such systems, it is useful to first introduce some fundamental concepts by considering the classic elastic localisation example of balloon inflation. Figure 1 illustrates a representative pressure-cross-sectional area relationship. Though derived from the structural mechanics of an elemental length of balloon, it is best thought of as a *material* response, analogous to a stress-strain relationship. Pressure is a generalised stress—which equilibrium demands must

be equal everywhere throughout the balloon—and area is a generalised strain—the integration of which along the length gives the generalised total displacement, the inflated volume. This relationship applies at every point along the length of the balloon, and, *if* the balloon were to inflate uniformly, scaling the area axis by the total length of the balloon would give the pressure-volume relationship; i.e. the load-displacement response. In reality during inflation, localisation occurs, and the deformation is non-uniform: Fig. 2 illustrates the corresponding pressure-volume relationship when a balloon of finite length is inflated under displacement control. As most of us have experienced, the balloon initially deforms uniformly, until a peak pressure, p_{max}, is reached; subsequently, deformation localises in a bulge—the high strain phase—which propagates along the balloon at a constant, lower, pressure, p^*. When the bulge reaches the end of the balloon, uniform deformation recommences and the pressure required for further inflation increases.

The Maxwell Equal-Areas construction was first derived to find phase mixtures in a van der Waals' fluid [7]. Ericksen [8] showed that the construction can be applied to a generalised stress-strain relationship to find the strains in each phase, which are the strains that minimise the total strain energy of the system. This is illustrated in Fig. 1: a horizontal line is drawn such that the areas 1 and 2, bounded by the line and the pressure curve, are equal, which sets the propagation pressure p^*, and associated cross-sectional areas A_A and A_B. For generalised stress and strain, the construction is stated as

$$\int_{\epsilon_\mathrm{A}}^{\epsilon_\mathrm{B}} \sigma \,\mathrm{d}\epsilon = \sigma^*(\epsilon_\mathrm{B} - \epsilon_\mathrm{A}) \tag{1}$$

where σ^* is the propagation stress, and ϵ_A and ϵ_B are the strains in the low- and high-strain phases respectively. In addition to balloons, the construction has been used in the analysis of buckling pipes [1], among other localisation problems; further overview of elastic localisation, including proofs of the Maxwell Equal-Areas construction, can be found in our other recent study [9].

Previous work has focused on homogeneous elastic domains, where the generalised stress-strain relationship does not vary with position along the domain, e.g. a balloon or a tape-spring with uniform cross-section along its length. We now wish to consider heterogeneous elastic domains, i.e. one-dimensional elastic systems with a spatially varying stress-strain relationship. In particular, we note that the Maxwell Equal-Areas Construction must be satisfied *specifically* on the boundary between the two phases, which was originally shown by Gurtin [10] for three dimensional domains, but has since featured in relatively little discussion. If the elastic domain is homogeneous with the same stress-strain relationship throughout, the distinction is irrelevant; however, for spatially varying relationships, the distinction is fundamental to understanding the localisation behaviour, which we intend to elucidate, by proof and by examples.

The first section of this paper presents a new simplified proof of Gurtin's result for one-dimensional elastic domains with spatially varying stress-strain relationships. The remainder considers systems with spatially varying stress-strain relationships, in particular, tape-springs with varying cross-section, which we call "tapered-springs". Tape-springs normally have uniform cross-

section and an homogeneous elastic domain. During bending they are able to localise deformation into a region known as a "fold", of concentrated, constant curvature [3], which is incompatible with certain highly coiled applications, leading to incorrect deployment. Such instability may be alleviated using tape-springs that are non-uniformly shaped.

The simplest prescriptions of a varying elastic domain consider special cases of constant subtended angle and constant width tapered-springs: this is Part I. A following Part II paper deals with more arbitrary variation of cross-sections, in particular, tapered-springs with non-monotonic subtended angle, which are shown to undergo an unusual fold propagation behaviour involving discrete "jumps" in the curvature of the fold.

2 Proof of Maxwell Equal-Areas Construction

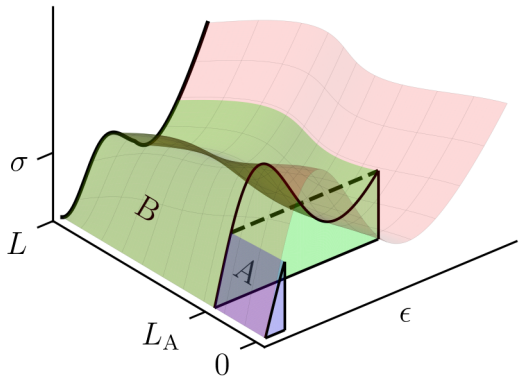

Figure 3: Strain energy diagram for an elastic domain with stress-strain relationship that varies along the length, and has localised into regions A (lower strain) and B (higher strain). The dashed line highlights that the horizontal stress plane in regions A and B is equal.

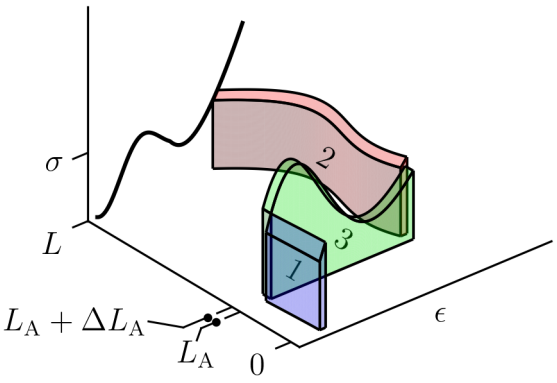

Figure 4: A small change in the length L_A resulting in changes in strain energy.

Consider a generalised, one-dimensional elastic domain, governed by a non-linear, non-monotonic "up-down-up" stress-strain relationship which varies spatially within the domain: values of stress and strain are always positive. By plotting this stress-strain "surface" according to Cartesian axes of stress vs strain vs length, a "strain energy diagram" is created, where the volume contained beneath the stress-strain "landscape" gives the total strain energy stored in the system, as shown in Fig. 3, and introduced by the authors in [9].

Let the length domain be divided into two phases: one, A, of near zero strain; and a second, B, of considerable strain. The volumes contained under the surface in regions A and B are equal

to the total strain energy in the system: additionally, the vertical projection of these regions onto the horizontal plane gives the total extension.

Though the generalised stress-strain relationship varies spatially throughout the domain, "local" equilibrium, of a small element of the domain, requires that the generalised stress is, everywhere, constant: this requirement is key to the analysis. For example, if the domain is an elastic rod with varying cross-sectional area, the appropriate generalised "stress" would be the force applied to its ends and carried axially. Similarly, "global" equilibrium must be satisfied; i.e. the configuration of phases are such that the total potential energy, $\Pi = U - V$, where U is the internal strain energy and V is the external work done, is minimised. Since localisation occurs under displacement control, the potential energy associated with the applied loads is fixed for a given displacement: therefore the elemental change in V is zero. Thus, minimising the total potential energy becomes equivalent to minimising the internal strain energy, U. To find the strains which minimise the total strain energy and, hence, achieve equilibrium, we must investigate a small change in the strains at a constant extension.

Consider a small increase in L_A, as illustrated in Fig. 4. Since the total extension must be constant, the strains $\epsilon_\mathrm{B}(x)$ in region B must increase, and, since the stress must be constant throughout the domain, there is a necessary increase in $\epsilon_\mathrm{A}(x)$. There are, therefore, three regions of change, numbered 1, 2 and 3: regions 1 and 2 are "gained", and region 3 is "lost". The constant extension requirement means there is no change of vertically projected area, thus

$$A_1 + A_2 = A_3 \tag{2}$$

At the minimum strain energy, there should be no change in strain energy under an incremental change in L_A. Therefore the total volume under the graph should be conserved, leading to

$$V_1 + V_2 = V_3 \tag{3}$$

Noting in the limit as ΔL_A tends to zero and, hence, as $\Delta\epsilon_\mathrm{A}(x)$ and $\Delta\epsilon_\mathrm{B}(x)$ tend to zero, the volumes 1 and 2 are given by

$$V_1 + V_2 = \sigma(A_1 + A_2) \tag{4}$$

Substituting Eqns 2 & 3 into the above, we arrive at

$$V_3 = \sigma A_3 \tag{5}$$

where

$$V_3 = \Delta L_\mathrm{A} \int_{\epsilon_\mathrm{A}(L_\mathrm{A})}^{\epsilon_\mathrm{B}(L_\mathrm{A})} \sigma(L_\mathrm{A}, \epsilon)\,\mathrm{d}\epsilon \tag{6}$$

and

$$A_3 = [\epsilon_{\mathrm{B}}(L_{\mathrm{A}}) - \epsilon_{\mathrm{A}}(L_{\mathrm{A}})]\Delta L_{\mathrm{A}} \tag{7}$$

Finally, dividing both sides by ΔL_{A}, this can be written as

$$\int_{\epsilon_{\mathrm{A}}(L_{\mathrm{A}})}^{\epsilon_{\mathrm{B}}(L_{\mathrm{A}})} \sigma(L_{\mathrm{A}}, \epsilon)\,\mathrm{d}\epsilon = \sigma[\epsilon_{\mathrm{B}}(L_{\mathrm{A}}) - \epsilon_{\mathrm{A}}(L_{\mathrm{A}})] \tag{8}$$

which is the Maxwell Equal-Areas Construction, specified on the phase boundary.

Formalising algebraically, the strain energy, U, is given by

$$U = \underbrace{\int_0^{L_{\mathrm{A}}} \int_0^{\epsilon_{\mathrm{A}}(x)} \sigma(x, \epsilon)\,\mathrm{d}\epsilon\,\mathrm{d}x}_{\text{Phase A}} + \underbrace{\int_{L_{\mathrm{A}}}^{L} \int_0^{\epsilon_{\mathrm{B}}(x)} \sigma(x, \epsilon)\,\mathrm{d}\epsilon\,\mathrm{d}x}_{\text{Phase B}} \tag{9}$$

where $\epsilon_{\mathrm{A}}(x)$ and $\epsilon_{\mathrm{B}}(x)$ are the strains in phases A and B respectively, $x = L_{\mathrm{A}}$ is the position of the phase boundary, and $\sigma(x, \epsilon)$ is the stress-strain relationship which varies throughout the domain.

Clearly, σ, L_{A}, $\epsilon_{\mathrm{A}}(x)$ and $\epsilon_{\mathrm{B}}(x)$ are *not* independent—the value of σ sets $\epsilon_{\mathrm{A}}(x)$ and $\epsilon_{\mathrm{B}}(x)$, and, for a given total extension, L_{A}. Minimisation of U can be performed with respect to any of the descriptive variables, and we choose to set $\mathrm{d}U/\mathrm{d}\sigma = 0$. Differentiating with respect to the stress σ throughout the domain by application of the Leibniz integral rule, we find:

$$\begin{aligned}\frac{\mathrm{d}U}{\mathrm{d}\sigma} = &\int_0^{\epsilon_{\mathrm{A}}(L_{\mathrm{A}})} \sigma(L_{\mathrm{A}}, \epsilon)\,\mathrm{d}\epsilon \frac{\mathrm{d}L_{\mathrm{A}}}{\mathrm{d}\sigma} + \int_0^{L_{\mathrm{A}}} \frac{\partial}{\partial\sigma}\left\{\int_0^{\epsilon_{\mathrm{A}}(x)} \sigma(x, \epsilon)\,\mathrm{d}\epsilon\right\}\mathrm{d}x \\ &+ \int_0^{\epsilon_{\mathrm{B}}(L)} \sigma(L, \epsilon)\,\mathrm{d}\epsilon \frac{\mathrm{d}L}{\mathrm{d}\sigma} - \int_0^{\epsilon_{\mathrm{B}}(L_{\mathrm{A}})} \sigma(L_{\mathrm{A}}, \epsilon)\,\mathrm{d}\epsilon \frac{\mathrm{d}L_{\mathrm{A}}}{\mathrm{d}\sigma} + \int_{L_{\mathrm{A}}}^{L} \frac{\partial}{\partial\sigma}\left\{\int_0^{\epsilon_{\mathrm{B}}(x)} \sigma(x, \epsilon)\,\mathrm{d}\epsilon\right\}\mathrm{d}x = 0\end{aligned} \tag{10}$$

Given the fixed length L of the domain, $\mathrm{d}L/\mathrm{d}\sigma = 0$, and combining the first and fourth integrands sets new limits for the first integral:

$$\begin{aligned}\frac{\mathrm{d}U}{\mathrm{d}\sigma} = &\int_{\epsilon_{\mathrm{B}}(L_{\mathrm{A}})}^{\epsilon_{\mathrm{A}}(L_{\mathrm{A}})} \sigma(L_{\mathrm{A}}, \epsilon)\,\mathrm{d}\epsilon \frac{\mathrm{d}L_{\mathrm{A}}}{\mathrm{d}\sigma} + \int_0^{L_{\mathrm{A}}} \frac{\partial}{\partial\sigma}\left\{\int_0^{\epsilon_{\mathrm{A}}(x)} \sigma(x, \epsilon)\,\mathrm{d}\epsilon\right\}\mathrm{d}x \\ &+ \int_{L_{\mathrm{A}}}^{L} \frac{\partial}{\partial\sigma}\left\{\int_0^{\epsilon_{\mathrm{B}}(x)} \sigma(x, \epsilon)\,\mathrm{d}\epsilon\right\}\mathrm{d}x\end{aligned} \tag{11}$$

Now, noting that

$$\frac{\partial}{\partial\sigma}\int_0^{\epsilon_{\mathrm{A}}(x)} \sigma(x, \epsilon)\,\mathrm{d}\epsilon = \sigma(x, \epsilon_{\mathrm{A}}(x))\frac{\mathrm{d}\epsilon_{\mathrm{A}}(x)}{d\sigma} + \int_0^{\epsilon_{\mathrm{A}}(x)} \frac{\partial}{\partial\sigma}\sigma(x, \epsilon)\,\mathrm{d}\epsilon = \sigma(x, \epsilon_{\mathrm{A}}(x))\frac{\mathrm{d}\epsilon_{\mathrm{A}}(x)}{d\sigma} \tag{12}$$

we can update the second and third integrals

$$\frac{\mathrm{d}U}{\mathrm{d}\sigma} = \int_{\epsilon_\mathrm{B}(L_\mathrm{A})}^{\epsilon_\mathrm{A}(L_\mathrm{A})} \sigma(L_\mathrm{A}, \epsilon)\,\mathrm{d}\epsilon \frac{\mathrm{d}L_\mathrm{A}}{\mathrm{d}\sigma} + \int_0^{L_\mathrm{A}} \sigma(x, \epsilon_\mathrm{A}(x)) \frac{\mathrm{d}\epsilon_\mathrm{A}(x)}{d\sigma}\,\mathrm{d}x + \int_{L_\mathrm{A}}^{L} \sigma(x, \epsilon_\mathrm{B}(x)) \frac{\mathrm{d}\epsilon_\mathrm{B}(x)}{d\sigma}\,\mathrm{d}x = 0 \quad (13)$$

where σ can be moved outside the x-wise integrations:

$$\frac{\mathrm{d}U}{\mathrm{d}\sigma} = \int_{\epsilon_\mathrm{B}(L_\mathrm{A})}^{\epsilon_\mathrm{A}(L_\mathrm{A})} \sigma(L_\mathrm{A}, \epsilon)\,\mathrm{d}\epsilon \frac{\mathrm{d}L_\mathrm{A}}{\mathrm{d}\sigma} + \sigma\left(\int_0^{L_\mathrm{A}} \frac{\mathrm{d}\epsilon_\mathrm{A}(x)}{d\sigma}\,\mathrm{d}x + \int_{L_\mathrm{A}}^{L} \frac{\mathrm{d}\epsilon_\mathrm{B}(x)}{d\sigma}, \mathrm{d}x\right) = 0 \quad (14)$$

The total extension, e, is given by

$$e = \int_0^{L_\mathrm{A}} \epsilon_\mathrm{A}(x)\,\mathrm{d}x + \int_{L_\mathrm{A}}^{L} \epsilon_\mathrm{B}(x)\,\mathrm{d}x \quad (15)$$

Differentiating with respect to σ

$$\frac{\mathrm{d}e}{\mathrm{d}\sigma} = \epsilon_\mathrm{A}(L_\mathrm{A}) \frac{\mathrm{d}L_\mathrm{A}}{\mathrm{d}\sigma} + \int_0^{L_\mathrm{A}} \frac{\partial \epsilon_\mathrm{A}(x)}{\partial \sigma}\,\mathrm{d}x + \epsilon_\mathrm{B}(L) \frac{\mathrm{d}L}{\mathrm{d}\sigma} - \epsilon_\mathrm{B}(L_\mathrm{A}) \frac{\mathrm{d}L_\mathrm{A}}{\mathrm{d}\sigma} + \int_{L_\mathrm{A}}^{L} \frac{\partial \epsilon_\mathrm{B}(x)}{\partial \sigma}\,\mathrm{d}x = 0 \quad (16)$$

Again, noting that $\mathrm{d}L/\mathrm{d}\sigma = 0$, the third term is zero, and the first and fourth are combined:

$$[\epsilon_\mathrm{A}(L_\mathrm{A}) - \epsilon_\mathrm{B}(L_\mathrm{A})] \frac{\mathrm{d}L_\mathrm{A}}{\mathrm{d}\sigma} + \int_0^{L_\mathrm{A}} \frac{\partial \epsilon_\mathrm{A}(x)}{\partial \sigma}\,\mathrm{d}x + \int_{L_\mathrm{A}}^{L} \frac{\partial \epsilon_\mathrm{B}(x)}{\partial \sigma}\,\mathrm{d}x = 0 \quad (17)$$

which is substituted into Eqn 14:

$$\frac{\mathrm{d}U}{\mathrm{d}\sigma} = \int_{\epsilon_\mathrm{B}(L_\mathrm{A})}^{\epsilon_\mathrm{A}(L_\mathrm{A})} \sigma(L_\mathrm{A}, \epsilon)\,\mathrm{d}\epsilon \frac{\mathrm{d}L_\mathrm{A}}{\mathrm{d}\sigma} + \sigma[\epsilon_\mathrm{B}(L_\mathrm{A}) - \epsilon_\mathrm{A}(L_\mathrm{A})] \frac{\mathrm{d}L_\mathrm{A}}{\mathrm{d}\sigma} = 0 \quad (18)$$

Finally, rearranging and removing the common factor gives

$$\int_{\epsilon_\mathrm{A}(L_\mathrm{A})}^{\epsilon_\mathrm{B}(L_\mathrm{A})} \sigma(L_\mathrm{A}, \epsilon)\,\mathrm{d}\epsilon = \sigma[\epsilon_\mathrm{B}(L_\mathrm{A}) - \epsilon_\mathrm{A}(L_\mathrm{A})] \quad (19)$$

i.e. the Maxwell Equal-Areas Construction must be satisfied at $x = L_\mathrm{A}$, the phase boundary.

Whilst we have shown that this condition leads to an equilibrium configuration, its stability has not been verified, and there remains the possibility that other equilibrium configurations exist; a proof of stability and uniqueness, or lack thereof, is left for future work. In homogeneous domains undergoing localisation, there are two equilibrium solutions: the localised configuration, which is stable, and uniform deformation, which is unstable when the strain is in the decreasing region of the stress-strain curve [9]: we may reasonably infer the localised solution in heterogeneous domains is also stable. In Part II, we will see examples of domains where Eqn 19 can be satisfied by more than one configuration of strains for a given total displacement, and hence multiple stable equilibrium

configurations are possible, but for the examples discussed in Part I, only one localised equilibrium configuration exists.

Such pertinent satisfaction was first shown by M E Gurtin for a general three dimensional elastic domain [10], using notation more familiar to those well versed in continuum mechanics, and is perhaps unsurprising if we consider a typical propagating instability analysis [9]: of course, the stress throughout the domain must equal the propagation stress at the boundary between phases, in order to propagate the high-strain phase through that region. It should be noted that the specification of the Maxwell Equal-Areas Construction on the boundary between phases is uniquely important to elastic localisation, where there is a well defined boundary and the stress-strain relationship is spatially fixed; in thermodynamic settings, due to the fluidity of liquids and gases, the domain is typically fairly homogeneous at a large scale.

The analysis in this Section pertains to elastic deformation, where localisation is reversible and the undeformed state fully recoverable. It does not apply to plastic deformations, for example, necking of ductile bars in tension, which, at cursory glance, may appear similar, or to localised shear band deformations which occur in metals, polymers, and the Earth's lithosphere [11]; nor does it apply to elastic systems in which deformation is characterised by more than one variable, e.g. the localised formation of a ruck in a rug appears at first to be a one-dimensional problem: however, there are in fact two relevant generalised strains, elastic compressive strains and geometric shorting due to transverse bending of the ruck [12].

3 Application to tapered-springs

Tape-springs are long straight strips with transverse curvature, of which the carpenter's metallic measuring tape is a familiar everyday example. Their uniform cross-section is typically characterised by a constant transverse radius r, subtended angle α, arc-width $b = \alpha r$, and shell thickness h, see Fig. 5. When bent along their length by applying equal and opposite rotations at either end, a tape-spring deforms stiffly with uniform curvature up to a peak load before buckling such that the longitudinal curvature localises in a fold region—the high-strain phase—characterised by high curvature and a flattened cross-section, adjoined by relatively undeformed regions of lower curvature—the low-strain phase: notably, the fold radius is approximately equal to the initial transverse radius, r [13]. Further end rotation is accommodated by lengthening, or "growth", of the fold region at a constant moment.

Tape-springs are used frequently as deployable booms in aerospace structures such as satellite antennae. The tape-spring is stored by coiling around a central hub, with the fold enveloping the entire length of the spring. In a coiled configuration of multiple layers, the thickness of the flattened cross-section necessitates a variation of fold radius throughout the coil, such that the resultant coil is a tightly packed spiral, thereby constraining the fold radius to be different from r: the outer layers may be at a radius $> r$, and the inner layers $< r$. Such disparity from the

"natural" fold radius, r, can be problematical: for example, a coiled spring is prone to the "50-pence" effect, where the outer layers, coiled at a radius $> r$, buckle into a configuration of multiple unfolded segments joined by folds of radius r, in a shape resembling the familiar British coin [15]. Apart from undesirable looser packing, where, for satellites, space is at a premium, unfurling is not smooth; as the tape-spring is deployed, the outer layers of the coil (which previously constrained the rest of the coil) are no longer present, and so the inner layers can expand closer to their natural fold radius of r in a process known as "blossoming" (or sometimes "blooming"), compounded when deploying an inertial payload. The hub rotation becomes uncorrelated from the tip deployment, and the tape-spring can fail to completely deploy [14].

One method of mitigating the 50-pence effect is by tailoring the braid angle of fibres in a tape-spring made from laminated composite [15]: this choice of material affords lightweighting and is electrically inert with respect to telecommunications. The fold radius depends on the braid angle and, by varying it along the length, the natural fold radius can be made to match the coiling radius. The question now is whether such an approach is possible with isotropic tape-springs, in which a variable fold radius can only be achieved by varying the cross-sectional geometry along the tape: these will be called "tapered"-springs for obvious reasons later. The instantaneous analytical moment-curvature relationship with respect to length varies and, thus, creates a practical example of localisation with a spatially varying stress-strain relationship.

3.1 Tape-spring mechanics

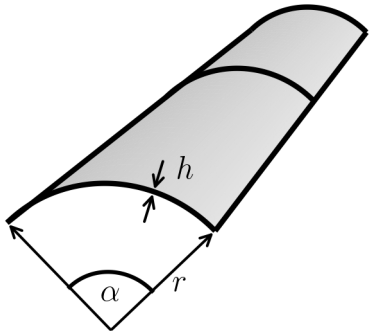

Figure 5: Tape-spring initial cross-section geometry.

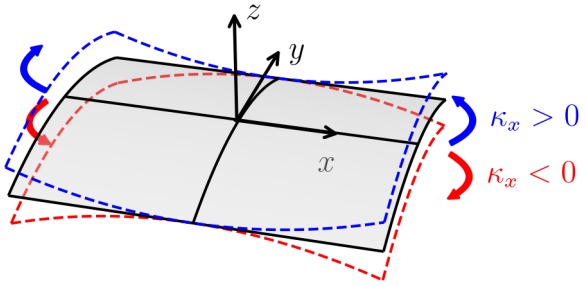

Figure 6: Deformation of an element of tape-spring under equal- ($\kappa_x < 0$) and opposite- ($\kappa_x > 0$) sense bending

Figure 6 illustrates the sign convention here for bending of a tape-spring or tapered-spring. Curvatures in the lengthwise x-direction and transverse y-direction are defined to be: $\kappa_x = \mathrm{d}^2z/\mathrm{d}x^2$, $\kappa_y = \mathrm{d}^2z/\mathrm{d}y^2$, where z is the displacement coordinate of the deformed surface; the initial, stress-

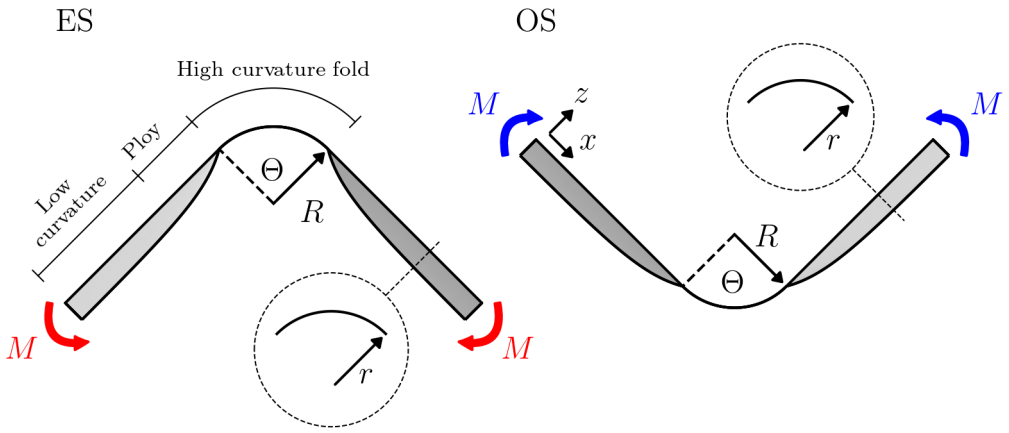

Figure 7: Tape-spring fold geometry in equal- and opposite-sense bending ("ES" and "OS"), with fold radius $R = 1/\kappa_x$, and flattened cross-section within the fold. Dashed circles illustrate the relatively undeformed cross-section in the low-curvature regions.

free transverse curvature κ_{y0} is always negative. Negative κ_x results in a mudguard-like form, and is termed "equal-sense" bending, whereas positive κ_x produces a saddle shape, in "opposite-sense" bending, which is associated with a positive bending moment. Figure 7 illustrates the side-view appearance of folds in standard tape-springs, typically forming in the middle of the tape-spring if we apply equal and opposite moments to either end: highlighted are the regions of low and high curvature, and the transitional "ploy" region.

Mansfield [16] produced an exact analytical solution for bending of a uniform tape-spring cross-section by solving the governing fourth-order differential equation in terms of the applied end moments, M, as a function of κ_x. The resulting solution is plotted in Fig. 8 for a typical cross-section geometry, and is non-linear, with the characteristic "up-down-up" shape of localisation problems: cross-section flattening accords the transition between an initial stiff beam-like response to a more flexible plate-like behaviour. The Maxwell Equal-Areas construction has been solved numerically and annotated in Fig. 8; by plotting the dimensionless curvature $\kappa_x r$, we see that κ_{xB} is close to unity, and the fold radius is fairly well approximated to r; note also that $\kappa_{xA} r = 0.002$, i.e. approximately zero.

Figure 9 plots the longitudinal curvature along the length of a folded tape-spring using a finite element analysis, following the approach described later in Section 3.4. In the ploy regions there is an oscillation in κ_x strongly reminiscent of Gibbs phenomenon familiar in Fourier series jumps, in which the change in transverse curvature decays rapidly.

The length-scale of the ploy depends on the cross-sectional geometry [17], and, in a standard tape-spring, remains constant as bending proceeds and the fold grows in length. The ploy features are, thus, invariant, and absent from any strain energy minimisation analysis, and from the Maxwell

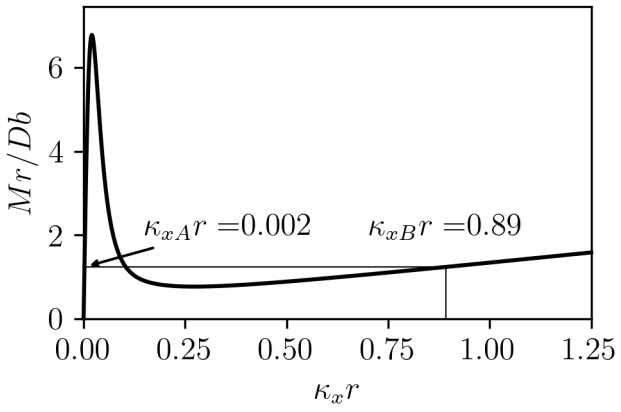

Figure 8: Analytical moment-curvature solution for a typical tape-spring cross-section in opposite sense bending, with the Maxwell Equal-Area construction applied.

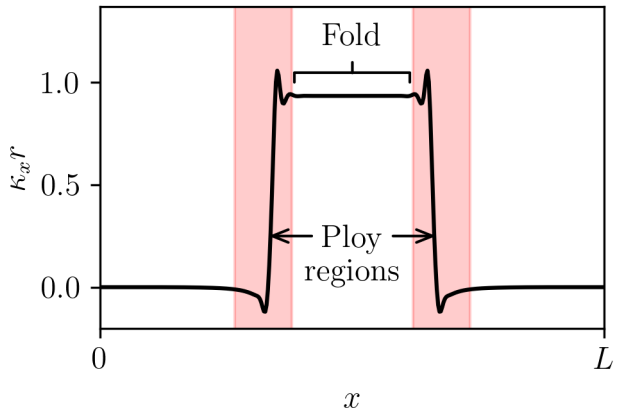

Figure 9: Longitudinal curvature along the length of a folded tape-spring, with the ploy regions highlighted.

Equal-Areas construction. However, the ploy does influence where folds will form, and whether one or two folds form: for a more detailed, "regularised", analysis of tape-spring folding, including the strain energy of the ploy region, we refer the reader to Martin et.al [18].

3.2 Maxwell construction in tape-springs

Using a simplified uniform curvature model of the fold region alone, Rimrott showed that the fold radius of a uniform tape-spring is (approximately) equal to the initial transverse radius r [19]. Later, Calladine & Seffen [20] took proper account of the free edge boundary conditions and improved the prediction of fold curvature, $\kappa_x = \kappa_{y0}/\xi$, where ξ is a value close to, but different from, unity, found by solving a characteristic equation.

However Calladine & Seffen's solution does not strictly satisfy the Equal-Areas construction because it does not account for the unfolded, nearly-straight parts. The solution was improved by the current authors by using a simple Euler beam approximation for the unfolded regions, and directly solving the Equal-Areas construction [9] to yield an augmented characteristic equation for ξ, as follows:

$$1 - \frac{1}{\xi^2} - \frac{A}{2}\left[3\xi^{1/2} - \frac{\nu^2}{\xi^{3/2}} \pm \frac{2\nu}{\xi^{1/2}}\right] + B\left[\frac{1}{\xi} \pm \nu\right]\left[\frac{1}{\xi} \pm \nu - \frac{A}{2}\left(\frac{3\nu^2}{\xi^{1/2}} - \xi^{3/2} \pm 2\nu\xi^{1/2}\right)\right] = 0 \quad (20)$$

where

$$A = \frac{2}{[3(1-\nu^2)]^{1/4}}\frac{1}{T}; \quad B = \frac{Db}{EI} = \frac{60}{(1-\nu^2)}\frac{1}{T^4} \quad (21)$$

and T is a non-dimensional parameter:

$$T = \sqrt{\frac{b^2}{rh}} \tag{22}$$

Note that A is the constant declared in [20], and B is a new constant [9].

The terms governed by the constant parameter B, represent the augmented form compared to the characteristic equation in terms of A. Since $A \propto 1/T$, and $B \propto 1/T^4$, it follows that: for very large T both A and B can be neglected, and the equation reduces to the Rimrott solution ($\xi = 1$); for intermediate T, only B can be neglected and the Calladine & Seffen solution is adequate; for small T, the full solution is required.

3.3 Tapered-spring fold curvature

Assuming zero transverse curvature, the moment in a tape-spring or a tapered-spring fold is approximately equal to

$$M = Db[\kappa_x \pm \nu\kappa_{y0}] \tag{23}$$

with $\pm$ for opposite- and equal-sense bending respectively. We propose to deal with tapered-springs of constant thickness h, and constant plate flexural stiffness D; therefore, we define a dimensionless moment, $m = M/D$, for compactness. For pure bending, m must be constant throughout the tapered-spring, setting

$$\kappa_x = \frac{m}{b} \mp \nu\kappa_{y0} \tag{24}$$

upon rearranging Eqn 23. The moment, m, must also observe the value that ensures the Maxwell Equal-Areas construction is satisfied at the propagating front of the fold. We therefore set $\kappa_x = \kappa_{y0}/\xi$ at the front of the fold, which we denote $x = L_f$, where L_f is the length of the fold, and ξ is calculated from Eqn 20; in other words

$$\kappa_x|_{L_f} = (\kappa_{y0}/\xi)|_{L_f} \tag{25}$$

3.4 Finite Element Model

The commercial finite element analysis (FEA) software package, Abaqus FEA [21], is used to model two tapered-springs: one with constant subtended angle, α, and the other with constant width, b, respectively shown in Figs 10 & 11; their cross-sections are illustrated at various points along the length for emphasising the variation of taper, and coloured by contours of displacement. To aid discussion henceforth, "inside", denoted by subscript "i", shall refer to the end with the smallest transverse radius r, and "outside", via subscript "o", to the end with the greatest.

The springs had the following geometric parameters: $r_\mathrm{o} = 20\,\mathrm{mm}$, $b_\mathrm{o} = 20\,\mathrm{mm}$, $r_\mathrm{i} = 14\,\mathrm{mm}$, $L = 200\,\mathrm{mm}$, resulting in $b_\mathrm{i} = 14\,\mathrm{mm}$ for the constant-α spring. A relatively common thickness of

$h = 0.15\,\text{mm}$ was used for the shell section, with material properties, $E = 120\,\text{GPa}$ and $\nu = 0.34$, of Copper Beryllium (CuBe), a common tape-spring material.

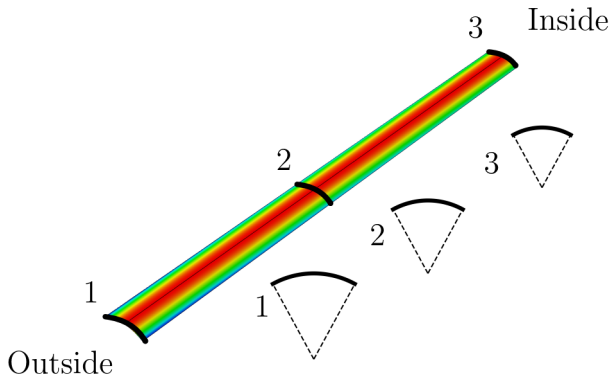

Figure 10: constant-α tapered-spring FEA model, coloured by z coordinate. The "outside" end is nearest, with a larger width and transverse radius.

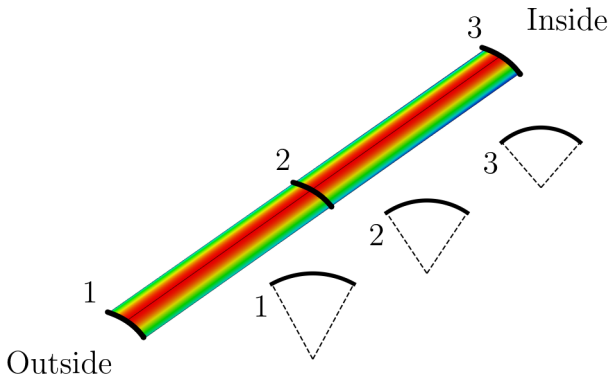

Figure 11: constant-b tapered-spring FEA model. The "outside" end is nearest, with a larger transverse radius.

For the constant-α spring, a symmetry boundary condition was applied on the inside end, where the fold initiates, allowing flattening of the cross-section but otherwise no displacements or rotations, whilst a rigid body "tie" was generated on the outside end. The nodes forming the tie are kinematically coupled, in that they rotate and displace identically; physically, they behave as a rigid body, enabling rotation to be applied at the moving end. For the constant-b spring, the symmetry boundary condition and rigid body tie swap position, as the fold now initiates at the outside. For computational efficiency and to enforce symmetrical folding, only half of the spring cross-section was modelled, with a symmetry boundary condition on the internal edge: 20 S4R5 reduced integration shell elements extend across the corresponding half-cross-section, and a stabilised static general step is used during a non-linear analysis. Only opposite-sense folding was considered since equal-sense bending can be accompanied by torsional buckling: otherwise, see [22].

3.5 Constant-α case

Simple Rimrott-like analytical models can be derived for a provisional comparison to FEA results. For the constant-α case, consider a linear variation in the initial transverse curvature, κ_{y0}, of the form

$$\kappa_{y0} = \kappa_{y,\text{out}}(1 + kx) \tag{26}$$

where k is an arbitrary constant, and $\kappa_{y,\text{out}}$ is the transverse curvature at the outside end, with extended subscript to clearly distinguish from κ_{y0}. Additionally, let b vary such that $\alpha = b\kappa_{y0}$ is constant. The fold curvature is, thus, required to be of the form

$$\kappa_x = \frac{m}{\alpha}\kappa_{y0} - \nu\kappa_{y0} = \left[\frac{m}{\alpha} - \nu\right]\kappa_{y0} \tag{27}$$

In the constant-α spring, the fold initiates at the inside, $x = L$. At the propagating front of the fold, which in this case is given by $x = L - L_f$, where L_f is the length of the fold, the Equal-Areas construction must be satisfied:

$$\kappa_x|_{L-L_f} = \frac{\kappa_{y0}|_{L-L_f}}{\xi|_{L-L_f}} \tag{28}$$

Therefore, m is given by

$$m = \alpha\left[1/\xi|_{L-L_f} + \nu\right] \tag{29}$$

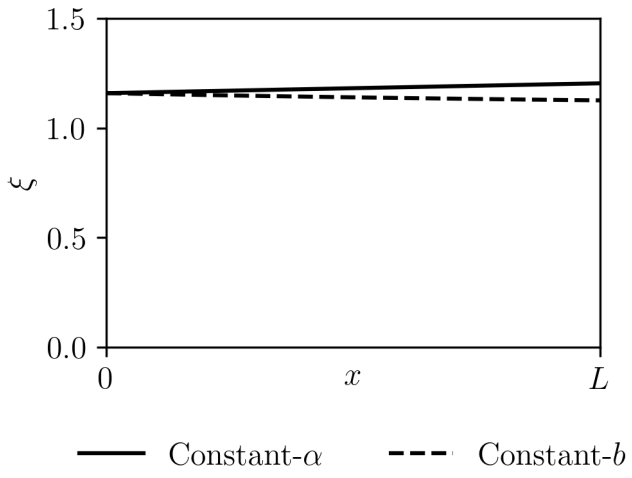

Figure 12: Variation in ξ along the constant-α and constant-b tapered-springs is minimal, and it is reasonable for the analytical expressions to assume ξ is constant.

We can obtain an expression for L_f by first finding Θ, which is given by the integral of fold curvature over the fold length, assuming ξ is constant along the tapered-spring—a reasonable assumption as illustrated by Fig. 12:

$$\Theta = \int_{L-L_f}^{L} \kappa_x \, \mathrm{d}x = \int_{L-L_f}^{L} \frac{\kappa_{y,\text{out}}}{\xi}\left(1 + kx\right) \, \mathrm{d}x = \frac{\kappa_{y,\text{out}}}{\xi}\left(L_f(1 + kL) - \frac{kL_f^2}{2}\right) \tag{30}$$

This yields a quadratic in L_f:

$$0 = \frac{k}{2}L_f^2 - (1+kL)L_f + \frac{\Theta\xi}{\kappa_{y,\text{out}}} \tag{31}$$

The roots are

$$L_f = \frac{(1+kL) \pm \sqrt{(1+kL)^2 - 2k\Theta\xi/\kappa_{y,\text{out}}}}{k} \tag{32}$$

where the negative root clearly gives the correct solution as L_f must grow with Θ.

3.5.1 FEA Results

Figure 13 shows the folding process for the constant-α spring. It is clear that the fold curvature *at a given position* is unchanged as deformation proceeds, as for standard tape-springs but in contrast to the second type of tapered-spring, later. The final fold, subtends an angle 540°, which can be seen in Fig. 14 as a clearly visible spiral.

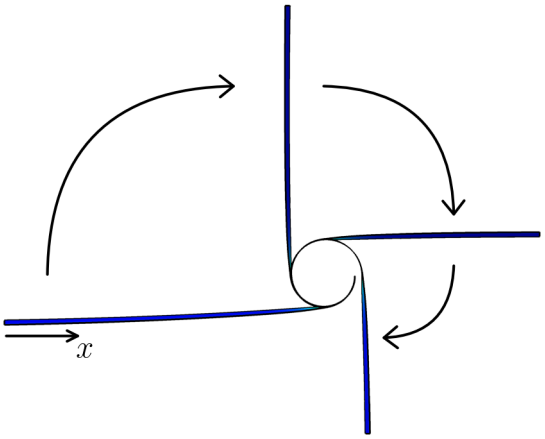

Figure 13: Folding of constant-α tapered-spring from $\Theta = 90°$ to 360°. Note the existing fold is unaffected by increases in Θ.

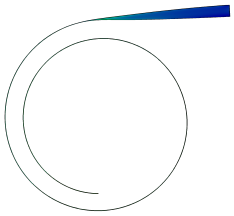

Figure 14: Final spiral fold formed by constant-α spring at $\Theta = 540°$.

Figure 15 shows the fold curvature along the centre-line of the tape-spring, for different total subtended angles, Θ. The fold initiates at the inside edge, on the inside of the resulting spiral; subsequently, the fold curvature lies perfectly on the Equal-Areas prediction, as the dash-dotted line in Fig. 15. Having formed, the curvature in the existing fold is not affected by the propagation process. The analytical solution, Eqns 27 & 32, plotted as dashed lines, agrees very well with the FEA results. The predicted propagating front lies within the FEA results ploy region, which is to be expected: L_f has been solved for the value of Θ from FEA; therefore, the area under both curves must be equal.

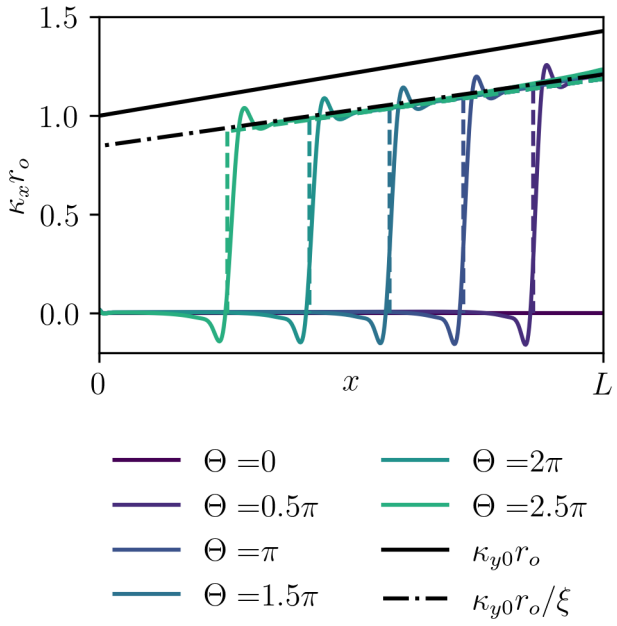

Figure 15: FEA fold curvature for constant-α; dashed lines indicate analytical solutions for κ_x, with the vertical portion showing the position of the propagating front. $x = 0$ is the outside end; $x = L$ the inside

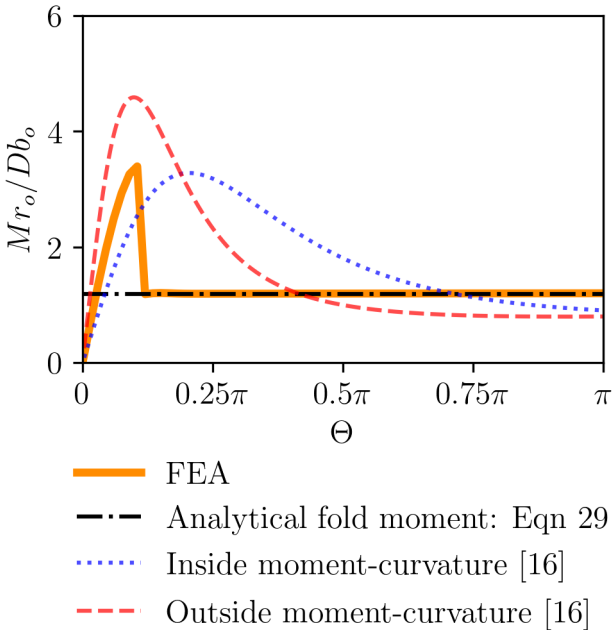

Figure 16: Moment-rotation plot for constant-α tapered-spring. The inside and outside cross-section moment-curvature analytical solutions are plotted assuming $\kappa_x = \Theta/L$.

Figure 16 shows the moment versus total subtended angle for the constant-α tapered-spring. Also included, for comparison, is Mansfield's analytical tape-spring bending solution for both the inside and outside end cross-sections [16]. The applied moments from FEA registers a maximum equal to the inside peak bending moment, whereupon the fold initiates at the inside end, since the rest of the spring can sustain a higher peak moment; furthermore, this part of the moment-rotation curve lies between the analytical moment-curvature profiles of the inside and outside cross-sections. In the plateau which follows, the fold has fully formed in the FEA, with a near-constant moment which closely matches the analytical prediction:

$$\frac{Mr_o}{Db_o} = \frac{1}{\xi} + \nu = \frac{1}{1.18} + 0.34 = 1.19 \tag{33}$$

from an approximate average value given by $\bar{\xi} = (\xi_o + \xi_i)/2 = (1.16 + 1.20)/2 = 1.18$.

3.6 Constant-b case

Consider the same linear variation of transverse curvature as previously, Eqn 26. If b is constant, the fold curvature is required to be of the form

$$\kappa_x = \frac{m}{b} - \nu\kappa_{y0} = \frac{m}{b} - \nu\kappa_{y,\text{out}}(1+kx) \tag{34}$$

In the constant-b spring, the fold initiates at the outside, $x = 0$. At the propagating front of the fold, $x = L_f$, satisfaction of the Equal-Areas construction requires that

$$\frac{m}{b} - \nu\kappa_{y,\text{out}}(1+kL_f) = \frac{\kappa_{y,\text{out}}(1+kL_f)}{\xi|_{L_f}} \tag{35}$$

Rearranging for m yields

$$m = b\kappa_{y,\text{out}}(1/\xi|_{L_f} + \nu)(1+kL_f) \tag{36}$$

Thus, m is a function of the fold length L_f, and, therefore, of the fold angle Θ, which is given by the integral of fold curvature over the fold length:

$$\Theta = \int_0^{L_f} \kappa_x \,\mathrm{d}x = \int_0^{L_f} \frac{m}{b} - \nu\kappa_{y,\text{out}}(1+kx)\,\mathrm{d}x = \frac{m}{b}L_f - \nu\kappa_{y,\text{out}}\left(L_f + \frac{kL_f^2}{2}\right) \tag{37}$$

Substituting Eqn 36 into Eqn 37 yields a quadratic in L_f:

$$0 = \left(k\kappa_{y,\text{out}}/\xi + \frac{\nu k\kappa_{y,\text{out}}}{2}\right)L_f^2 + (\kappa_{y,\text{out}}/\xi)L_f - \Theta \tag{38}$$

Once again assuming ξ is constant along the tapered-spring, the roots are

$$L_f = \frac{-\kappa_{y,\text{out}}/\xi \pm \sqrt{(\kappa_{y,\text{out}}/\xi)^2 + 4\left(k\kappa_{y,\text{out}}/\xi + \nu k\kappa_{y,\text{out}}/2\right)\Theta}}{2\left(k\kappa_{y,\text{out}}/\xi + \nu k\kappa_{y,\text{out}}/2\right)} \tag{39}$$

The positive root clearly gives the correct solution as L_f must grow with Θ. Dividing by $\kappa_{y,\text{out}}$, the expression simplifies to

$$L_f = \frac{-1/\xi + \sqrt{1/\xi^2 + 2(2/\xi+\nu)k\Theta/\kappa_{y,\text{out}}}}{2k/\xi + \nu k} \tag{40}$$

The corresponding moment can be shown to be

$$m = b\kappa_{y,\text{out}}(1/\xi+\nu)\left(\frac{1/\xi + \nu + \sqrt{1/\xi^2 + 2(2/\xi+\nu)k\Theta/\kappa_{y,\text{out}}}}{2/\xi+\nu}\right) \tag{41}$$

3.6.1 FEA Results

Figure 17 shows the folding process for the constant-b spring. The fold curvature at a given position can be seen to increase—a tightening of the fold—as the applied end rotation increases, alongside the fold growing in length. This contrasts with the constant-α spring, where the fold curvature at a given position is unchanged with increasing end rotation. Additionally, in the final fold subtending $\Theta = 540^\circ$ in Fig. 18, the spiral form, though present, is far less obvious than in the constant-α spring (Fig. 14). This effect is due to the factor of $-\nu$ on the initial curvature gradient in Eqn 34: since ν is typically small, 0.34 in this case, the fold curvature gradient is lessened. Further, and perhaps un-intuitively, the minus sign inverts the gradient: the "outside" end of the tape-spring, with the larger transverse radius, becomes the inside of the fold and vice versa—in contrast, again, to the constant-α spring.

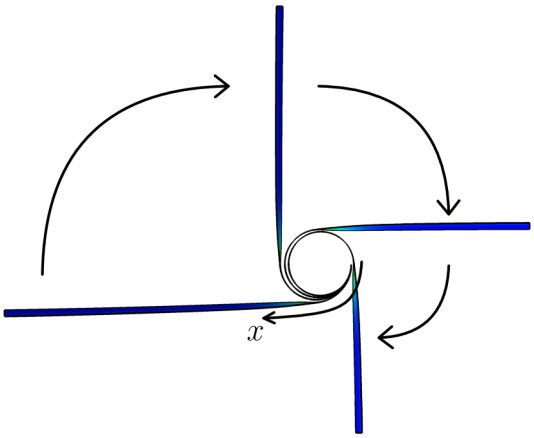

Figure 17: Folding process for constant-b tape-spring from $\Theta = 90^\circ$ to 360°. Note the contraction in the fold with increasing Θ.

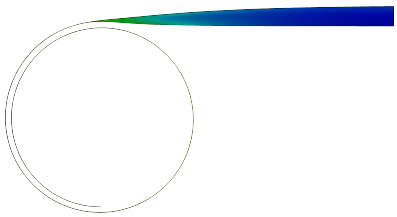

Figure 18: Final spiral fold formed by constant-b spring at $\Theta = 540^\circ$.

Figure 19 shows the fold curvature along the length of the constant-b tapered-spring, for different total subtended angles Θ. In contrast to the constant-α spring, the fold initiates at the outside end and subsequently progresses towards the inside end. The fold curvature evidently matches the required form, Eqn 24, and the Equal-Areas construction is satisfied at the propagating front of the fold. The analytical solution, Eqns 34 & 41, plotted as dashed lines, agrees well with the FEA results, predicting only slightly lower curvature, and identical gradient: as in Fig. 15, the analytical propagating front lies within the FEA ploy region.

Figure 20 shows the FEA moment versus total subtended angle for the constant-b tapered-spring, with moment-curvature profiles via Mansfield's solution for the inside and outside cross-sections, along with the analytical fold moment. As with Fig. 16, the FEA curve lies between the two cross-section solutions as far as the peak moment, after which the fold forms. For this

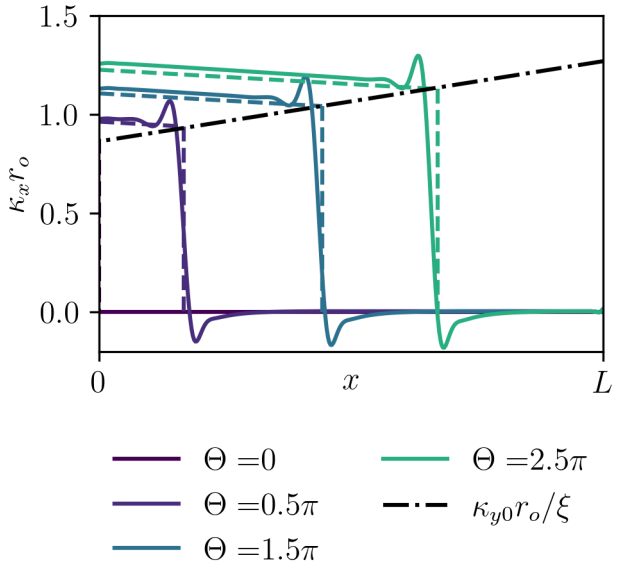

Figure 19: FEA fold curvature for constant-b spring; dashed lines indicate analytical solutions for κ_x, with the vertical portion showing the position of the propagating front. $x = 0$ is the outside end; $x = L$ the inside.

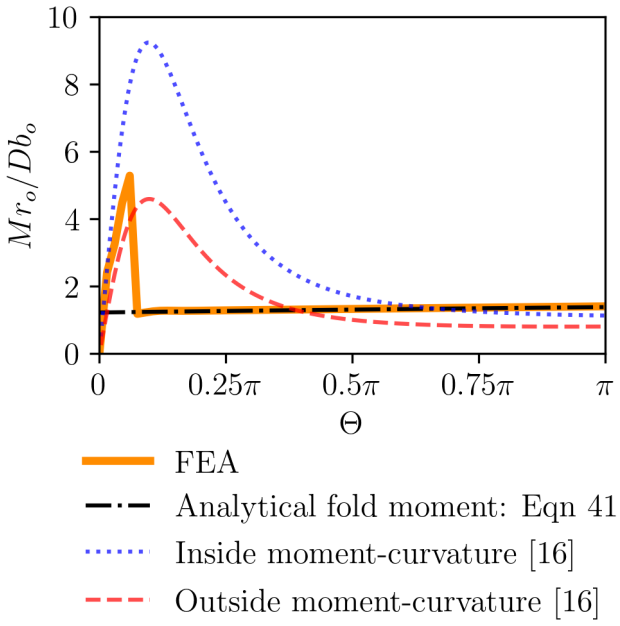

Figure 20: Moment-rotation plot for constant-b tapered-spring.

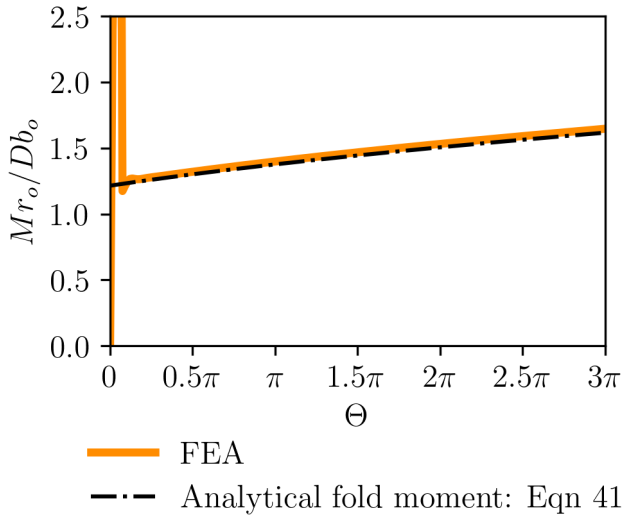

Figure 21: Moment-rotation plot for constant-b tapered-spring, with focus on fold moment.

tape-spring, the maximum attainable moment is governed by the outside cross-section, and is just

slightly less than the FEA peak value; hence, the fold initiates at the outside. Once the fold has formed, the FEA fold moment agrees very closely with the analytical fold solution; and continues to do so over a greater range of rotation, see Fig. 21.

In each of these cases, the fold location can be predicted exactly, in contrast to a standard tape-spring, where we must consider the strain energy associated with the ploy regions in order to predict the fold location [18].

3.7 Physical models

The manufacturing process for tapered-springs is similar to that of standard metal tape-springs: flat strips to give correct proportions that are then age-hardened to set the out-of-plane shape. First, the required shape is cut from a sheet of 0.15 mm thick CuBe; a trapezium for the constant-α spring and rectangle for the constant-b spring. For the constant-α spring, the width must vary in proportion with the radius of the steel cone used in the mould. The sheet cut-out is then positioned on top of two steel rods which are angled such that they run parallel to each edge of the sheet. The steel truncated cone forming the top half of the mould is then positioned on top of the sheet, and clamped down onto the sheet and rods by means of a third rod running through the middle of the cone - thus imparting the required curvature to the sheet. Figure 22 illustrates the mould setup with all clamps in place. The mould is then placed in an oven and the CuBe age-hardened at 350°C for three hours. Once cooled, the mould is disassembled, and the tapered-spring removed. Figure 23 shows two manufactured tapered-springs lying flat on a surface.

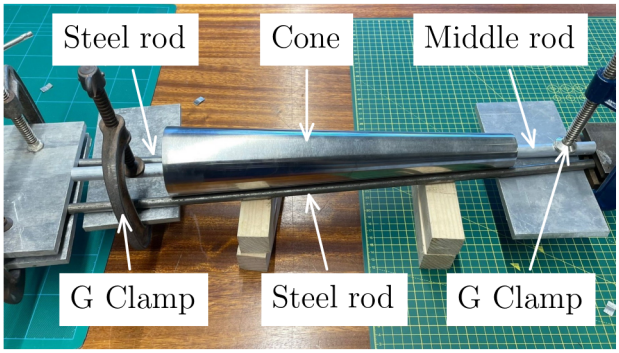

Figure 22: Mould assembled pre age-hardening. Thick metal plates are used to aid clamping the rods together.

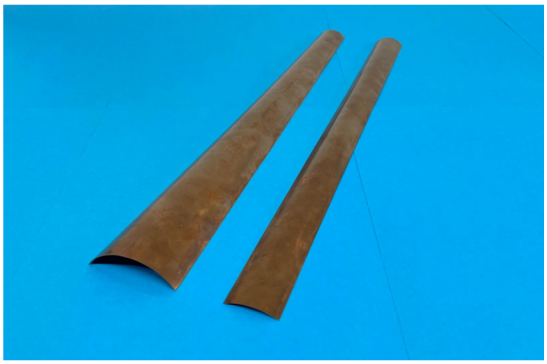

Figure 23: Constant-α spring on the left, constant-b on the right. For both springs the end with largest transverse radius is nearest; the opposite ends are identical in cross-section.

By re-purposing a steel truncated cone used for jewellery making, we are able to manufacture tapered-springs of reasonable conical geometry. The cone has maximum radius 38.1 mm, minimum

radius 19.7 mm, between a length of 380 mm. Two tapered-springs are manufactured, both of length 380 mm: a constant-α spring with $\alpha = \pi/2$, therefore $b_\mathrm{o} = 60\,\mathrm{mm}$ and $b_\mathrm{i} = 31\,\mathrm{mm}$; and constant-$b$ spring with $b_\mathrm{i} = b_\mathrm{o} = 31\,\mathrm{mm}$, therefore α varying from $\pi/2$ to $\pi/4$. However, age-hardening of tape-springs increases the transverse curvature relative to the mould, necessitating a measurement of the tapered geometry for accuracy. Denoting W as the cross-section width (where b is the arc width), and H the cross-section height, the manufactured subtended angle α can be calculated from

$$H = \frac{b}{\alpha}\,(1 - \cos\alpha/2)\,; \qquad W = \frac{2b}{\alpha}\sin\alpha/2 \tag{42}$$

The calculated values of α are given in Tables 1 & 2, and are consistently higher than the mould values. There is reasonable agreement between α as determined from H and W, signifying a close arc-like cross-section.

α	Mould	From H	From W
Outside	1.57	1.95	1.97
Inside	1.57	1.89	1.75

Table 1: constant-α spring geometry

α	Mould	From H	From W
Outside	0.79	0.98	1.07
Inside	1.57	1.93	1.73

Table 2: constant-b spring geometry

It is straightforward to form a fold by manually rotating each end of either spring in opposite directions. The fold can be made to travel along the length of spring in either direction, relatively smoothly; the fold radius also changes from r_o to r_i and vice-versa. In the constant-α spring, the fold travels freely in either direction, at a constant moment. In contrast, the constant-b fold prefers strongly to move towards the r_o end where the fold moment is lower.

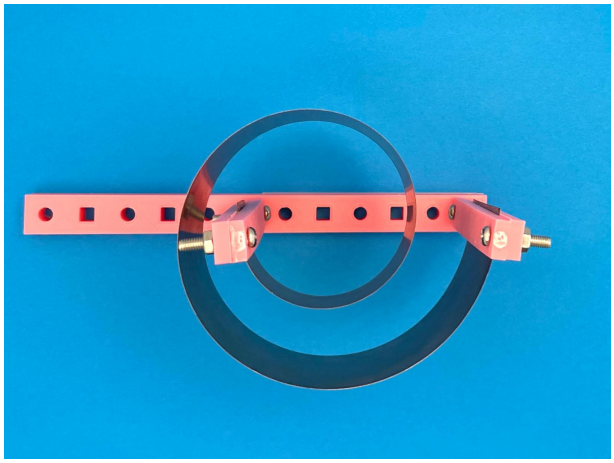

Figure 24: constant-α tapered-spring fold. Note that the close-up perspective gives the false appearance of a thick cross-section, which in reality is extremely thin.

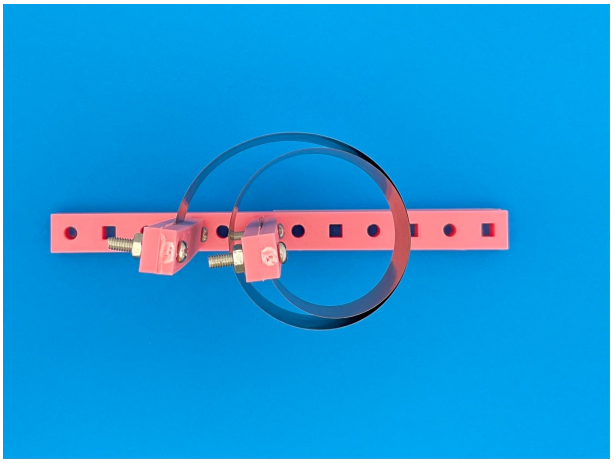

Figure 25: constant-b tapered-spring fold.

A simple demonstration of the completely folded tapes, which are held in bespoke 3D-printed

end grips, is given in Figs 24 & 25. It should be noted that these are not "perfect" folds as the applied loading is unlikely to be a pure moment. Nevertheless, it usefully confirms that the folds formed are spiral in nature, and that the constant-α fold is a much "looser" spiral with greater variation in its fold curvature. In theory, the constant-α outside fold radius is twice the value of the inside radius, and this appears to be so in Fig. 24.

4 Conclusions

We have given an alternative derivation of the condition by which the Maxwell Equal-Areas construction must be satisfied for localisation in a one-dimensional spatially varying elastic domain: specifically, the construction must be satisfied on the boundary between phases.

Practical examples that engage localisation are uniformly shaped tape-springs and their spatially varying counterparts that we called tapered-springs: under applied end rotations, curvature localises in hinge-like "fold" regions. The characteristically flattened cross-section allows the development of simple analytical models relating the fold curvature to bending moment, whilst their detailed mechanics and deformed geometry are reliably captured exactly by finite element analysis: this has enabled us to confirm the expected fold propagation behaviour. The Maxwell Equal-Areas construction must be satisfied on the propagating front of the fold, which determines the bending moment throughout the tapered-spring, and ultimately the variation of its fold curvature: when the transverse curvature varies linearly in tapered-springs, we have observed spiral-shaped folds.

Of particular interest is the case where the transverse subtended angle α is constant along the length: the fold moment and its curvature remain constant at a given position as the fold propagates. In contrast, when α varies along the length, the fold moment and its curvature vary as the fold propagates. A method has been devised for manufacturing these springs from Copper Beryllium using a conical mould geometry. These tapered-springs may have beneficial application in deployable structures, alleviating instabilities commonly observed when coiling standard tape-springs.

Whilst tapered-springs have been investigated here as a specific example, the principles are general, and apply to all one-dimensional elastic systems with spatially varying domains which exhibit a characteristic "up-down-up" relationship between its generalised stress, i.e. from loading, and strain, i.e. deformation. There is, therefore, great scope for synthesising other examples of such systems in the future; in particular, those where, like tapered-springs, the generalised stress-strain relationship is a function of the local geometry, which is much easier to manipulate than the fundamental material properties, such as 3D-printed meta-materials. Part II of this work gives suitable demonstration.

The authors would like to thank the EPSRC and StructureMode for funding this research through the EPSRC Centre for Doctoral Training in Future Infrastructure and Built Environment: Resilience in a Changing World (EPSRC grant reference number EP/S02302X/1).

References

[1] E Chater and J W Hutchinson, On the Propagation of Bulges and Buckles, (1984) *Journal of Applied Mechanics*, 51(2), pp. 269–277

[2] T A Netto and S Kyriakides and X Ouyang, On the Initiation and Propagation of Buckles in a Beam on a Nonlinear Foundation, (1999) *Journal of Applied Mechanics*, 66(2), pp. 418-426

[3] K A Seffen and S Pellegrino, Deployment dynamics of tape-springs, (1999) *Proceedings of the Royal Society of London. Series A: Mathematical, Physical and Engineering Sciences*, 455(1983), pp. 1003-1048

[4] A T Price and S Chapman, I. A mathematical discussion on the structure of wood in relation to its elastic properties, (1929) *Philosophical Transactions of the Royal Society of London. Series A, Containing Papers of a Mathematical or Physical Character*, 228, pp. 1-62

[5] H X Zhu and J R Hobdell and A H Windle, Effects of cell irregularity on the elastic properties of 2D Voronoi honeycombs, (2001) *Journal of the Mechanics and Physics of Solids*, 49(4), pp. 857-870

[6] M Fleisch and A Thalhamer and G Meier and I Raguž and P F Fuchs and G Pinter and S Schlögl and M Berer, Functional mechanical metamaterial with independently tunable stiffness in the three spatial directions, (2021) *Materials Today Advances*, 11

[7] J Clerk-Maxwell, On the Dynamical Evidence of the Molecular Constitution of Bodies, (1875) *Journal of the Chemical Society*, 28(0), pp. 493–508

[8] J L Ericksen, Equilibrium of bars, (1975) *Journal of Elasticity*, 5(3-4), pp. 191–201

[9] J A Clarkson and K A Seffen, Elastic Localisation With Particular Reference to Tape-Springs, (2024) *Journal of Applied Mechanics*, 91(12), pp. 121003-1-10

[10] M E Gurtin, Two-phase deformations of elastic solids, (1983) *Archive for Rational Mechanics and Analysis*, 84(1), pp. 1-29

[11] D Bercovici and S Karato, Theoretical Analysis of Shear Localization in the Lithosphere, (2002) *Reviews in Mineralogy and Geochemistry*, 51 (1), pp. 387–420

[12] A A Lee and and C Le Gouellec and D Vella, The role of extensibility in the birth of a ruck in a rug, (2015) *Extreme Mechanics Letters*, 5, pp. 81-87

[13] C R Calladine, The Theory of Thin Shell Structures 1888–1988, (1988) *Proceedings of the Institution of Mechanical Engineers, Part A: Power and Process Engineering*, 202(3), pp. 141-149

[14] J M Fernandez and M Schenk and G Prassinos and V J Lappas and S O Erb, Deployment Mechanisms of a Gossamer Satellite Deorbiter, (2013) *Paper presented at 15th European Space Mechanisms and Tribology Symposium*

[15] J M Fernandez and A Viquerat and V J Lappas and A J Daton-Lovett, Bistable Over the Whole Length (BOWL) CFRP Booms for Solar Sails, (2014) *Advances in Solar Sailing*, pp. 609-628

[16] E H Mansfield, Large-Deflexion Torsion and Flexure of Initially Curved Strips, (1973) *Proceedings of the Royal Society of London. Series A*, 334(1598), pp. 279-298

[17] B Wang and K A Seffen and S D Guest, Folding of Bistable Composite Tape-Springs, (2019) CUED/D-STRUCT/TR.252

[18] M Martin and S Bourgeois and B Cochelin and F Guinot, Planar folding of shallow tape-springs: The rod model with flexible cross-section revisited as a regularized Ericksen bar model, (2020) *International Journal of Solids and Structures*, 188-189, pp. 189-209

[19] F P J Rimrott, Querschnittsverformung bei Torsion Offener Profile, (1970) *ZAMM-Journal of Applied Mathematics and Mechanics/Zeitschrift für Angewandte Mathematik und Mechanik*, 50(12), pp. 775-778

[20] C R Calladine and K A Seffen, Folding the Carpenter's Tape: Boundary Layer Effects, (2020) *Journal of Applied Mechanics*, 87(1), pp. 011009-1-5

[21] M Smith, ABAQUS/Standard User's Manual, Version 6.9., (2009) *Dassault Systèmes Simulia Corp*

[22] J A Clarkson and K A Seffen, Torsional buckling of a tape-spring: Review and renew, (2024) *International Journal of Solids and Structures*, 302, pp. 112992-1-12